Progress In Electromagnetics Research M, Vol. 136, 1–12, 2025 PIER M

(Received 13 July 2025, Accepted 6 October 2025, Scheduled 30 October 2025)

Coin-Sized Dual-Band Millimeter-Wave (mmWave) Antenna with Machine-Learning-Guided Impedance Prediction

Ahmed J. A. Al-Gburi*

Center for Telecommunication Research & Innovation (CeTRI)
Fakulti Teknologi Dan Kejuruteraan Elektronik Dan Komputer (FTKEK)
Universiti Teknikal Malaysia Melaka (UTeM), Jalan Hang Tuah Jaya, Durian Tunggal, Melaka 76100, Malaysia

ABSTRACT: This study proposes a coin-sized ($12 \times 8 \times 0.64\,\text{mm}^3$) millimetre-wave antenna that simultaneously resonates at 28 GHz and 38 GHz and is supported by a machine-learning surrogate model for near-instant impedance evaluation. Realised on a Rogers 6010LM laminate ($\varepsilon_r = 10.2$), the radiator maintains $|S_{11}| \leq -10$ dB across 26.5–29.9 GHz and 37.2–39.7 GHz, providing peak gains of 3.8 dBi and 4.1 dBi at the lower and upper bands, respectively. A design-of-experiments sweep comprising 330 full-wave simulations generated the training corpus for a random-forest regression model. The surrogate predicts frequency-resolved $|S_{11}|$ with a mean-absolute error below 0.7 dB and coefficients of determination of 0.93 at 28 GHz and 0.84 at 38 GHz. The evaluation time is reduced from approximately 155 s per full-wave electromagnetic simulation to 0.1 s per surrogate query, enabling real-time design exploration. Eight-fold cross-validation confirms model stability, while feature-importance analysis identifies the geometric parameters most influential to dual-band matching. The learning-guided workflow therefore offers a fast and reliable alternative to exhaustive simulation, accelerating the optimisation of compact mmWave antennas for instrumentation, sensing, and future front-end modules.

1. INTRODUCTION

The accelerated opening of the millimetre-wave (mmWave) spectrum — most notably the 28 GHz (n257/n258) and 38 GHz (n260) bands — has intensified the quest for ultra-compact, high-performance radiators that overcome severe path loss while fitting into footprints of only a few square millimetres [1–3]. Although recent dual-band prototypes achieve this size target, they typically require dozens or even hundreds of full-wave sweeps to achieve concurrent impedance matching, leaving the design cycle slow, computationally expensive, and energy-intensive.

A close reading of contemporary literature reveals five main hardware directions shaping this miniaturised mmWave space. Tiwari et al. [4] introduced a dual-slot patch on flexible Rogers 3003 that maintains 28/38 GHz operation under mechanical bending, making it viable for conformal and biomedical surfaces. Ullah et al. [5] pushed miniaturisation further by embedding a split-ring/closed-ring metamaterial pair in a 6 mm × 8 mm board, widening each band and forming two spatially separated beams to mitigate blockage. Liang et al. [6] tackled dense integration by co-locating four steerable 28 GHz arrays and two sub-6 GHz elements within a single aperture, while Oh et al. [7] exploited unused bezel space by folding a coplanar-waveguide dipole into a $0.03\lambda_0$-high OLED rim, still achieving 12.3 dBi gain and more than 54% efficiency. Khabba et al. [8] expanded this concept with a three-dimensional phased-array architecture that stacks 5 mm × 6 mm × 0.8 mm patch elements around a device perimeter, achieving 16.1 dB gain, > 50 dB isolation, and full 360° steering across 24–28 GHz while preserving motherboard area. Collectively, these works trace a trajectory from bend-tolerant patches and aggressive footprint reduction to aperture sharing and volumetric beam-forming, each mitigating mmWave loss and blockage while conserving valuable real estate.

Parallel to these hardware advances, machine-learning (ML) surrogates have emerged as a powerful software remedy, learning the nonlinear relationship between geometry and performance from limited high-fidelity simulations and replacing hour-long electromagnetic (EM) with millisecond inference. Ensemble and deep-learning models have already driven mean-absolute errors below 1 dB and achieved speed-ups exceeding two orders of magnitude when predicting gain, directivity, or S-parameters of larger arrays [9–13]. Recent studies have expanded this trend: CatBoost and Gradient Boosting models have achieved high-accuracy return-loss prediction for internet of things (IoT) antennas, significantly reducing design time [14]; deep learning networks have been shown to outperform classical models (support vector machine (SVM), K-nearest neighbor (KNN), multilayer perceptron (MLP)) in predicting metamaterial antenna bandwidth with minimal MSE [15]; and comprehensive reviews confirm that reinforcement learning, genetic algorithms, and hybrid PSO-ML frameworks are enabling fast, data-efficient design optimization for high-frequency antennas [16]. However, there remains a gap in the literature: no existing work simultaneously demonstrates (i) a truly coin-sized footprint (∼10 mm × 8 mm), (ii) dual-band operation covering both 28 GHz and 38 GHz

---

* Corresponding author: Ahmed Jamal Abdullah Al-Gburi (ahmedjamal@utem.edu.my, ahmedjamal@ieee.org).

doi:10.2528/PIERM25071303 Published by THE ELECTROMAGNETIC ACADEMY

TABLE 1. Mm-Wave antenna specification.

Antenna specification	Value (mm)	Antenna specification	Value (mm)
W	8.0	S_1	0.6
L	12.0	S_2	0.9
K_1	0.6	S_3	0.8
K_2	1.88	K_4	1.4
K_3	2.4	K_5	1.0
G_W	1.4	-	-

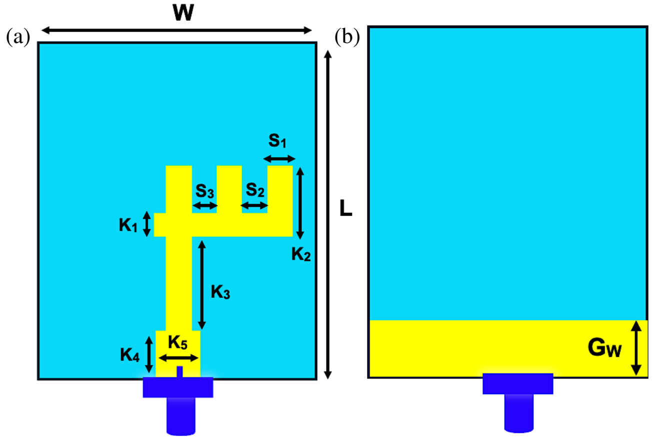

FIGURE 1. Predicated layout and dimensions of the modelled mmWave antenna: (a) patch view and (b) ground view.

bands, and (iii) a fast, frequency-resolved $|S_{11}|$ surrogate capable of millisecond-level inference.

This study directly addresses that gap. I present a 12 mm $\times$ 8 mm $\times$ 0.64 mm dual-band antenna fabricated on Rogers 6010LM, paired with a random-forest surrogate trained on 330 carefully sampled full-wave simulations. The model delivers mean-absolute error ≤ 0.7 dB, R$^2 \approx 0.9$ and inference time of only 0.1 s — over 150× faster than conventional EM sweeps. Cross-validation confirms model robustness, while feature-importance analysis reveals the geometric parameters most responsible for dual-band matching, providing actionable guidelines for rapid retuning and design reuse. Together, these contributions establish a practical route to real-time impedance assessment and agile optimisation of coin-sized mmWave antennas for next-generation measurement, sensing, and radio frequency front-end platforms.

2. MILLIMETER-WAVE ANTENNA DESIGN PROCEDURE

2.1. Millimeter-Wave Printed Antenna Design

The antenna is designed in this study employing Computer Simulation Technology (CST) Microwave Studio and implemented on a Rogers 6010LM substrate, which has a relative permittivity (ε_r) of 10.2 and a thickness of 0.64 mm. The overall size of the antenna structure is a coin-sized, measuring $12 \times 8 \times 0.64$ mm^3, making it highly suitable for the integration in modern miniaturized 5G systems. The antenna geometry and detailed layout are introduced in Fig. 1.

The radiating element consists of three vertical strips of varying lengths, arranged in a fork-like configuration and connected to a central feedline. This configuration is specifically engineered to support dual-band operation at 28 GHz and 38 GHz. The different strip lengths are responsible for generating multiple resonances, contributing to the wide operational bandwidth and stable radiation characteristics. The ground plane is located on the opposite side of the substrate and is extended to ensure proper impedance matching and radiation control. The full mmWave antenna geometry is recorded in Table 1.

The antenna is excited via a standard 50-ohm SMA connector through a microstrip feedline, which is optimized for minimal reflection and efficient energy transfer. The specific shape and dimensions of the strips were determined through parametric optimization to achieve high gain, low return loss, and desirable radiation performance at the target mm-wave bands.

The antenna was developed through a five-stage evolutionary process (Fig. 2). Starting with a single vertical-strip monopole (Configuration 1), successive iterations add resonant branches that broaden the impedance bandwidth and realise dual-band operation. Configuration 2 introduces a short horizontal stub, giving a modest bandwidth extension, while Configuration 3 employs two side branches that markedly lower $|S_{11}|$ around 28 GHz. Additional parasitic elements in Configurations 4 and 5 create well-defined resonances at both 28 GHz and 38 GHz. Simulated $|S_{11}|$ curves in Fig. 3 confirm the benefit of each modification: every step deepens the reflection-coefficient nulls, and the final design (Configuration 5) achieves minima of -36 dB at 28 GHz and -31 dB at 38 GHz. This multi-branch topology therefore combines a coin-sized 10×8 mm^2 footprint with wide impedance bandwidth and the high performance demanded by 5G mm-wave systems.

3. FABRICATION AND MEASUREMENT RESULTS

At this stage, the millimetre-wave printed antenna has been fabricated and experimentally validated. To maintain a coin-sized form factor, the design uses a Rogers 6010LM substrate whose high relative permittivity ($\varepsilon_r = 10.2$) and slim 0.64 mm thickness boost performance. Fig. 4 shows the fabricated prototype.

The reflection coefficient ($|S_{11}|$) was characterised with a Keysight FieldFox N9951A hand-held vector network analyser

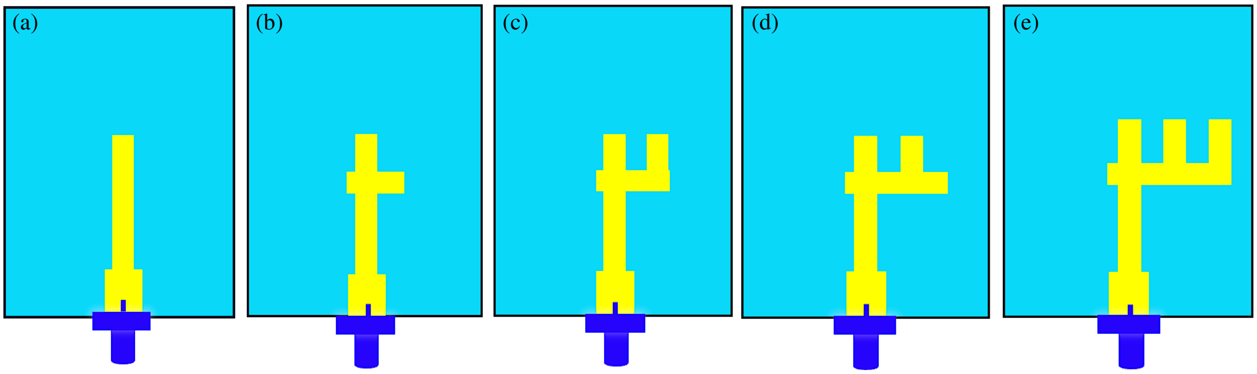

FIGURE 2. Simulated reflection-coefficient ($|S_{11}|$) responses for the five progressive configurations.

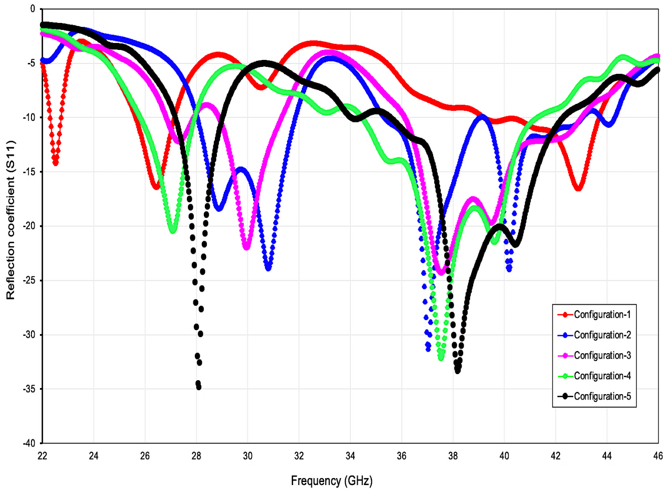

FIGURE 3. Simulated S_{11} results for the five antenna configurations. Progressive design steps enhance impedance matching and bandwidth, with Configuration 5 achieving deep dual-band resonances.

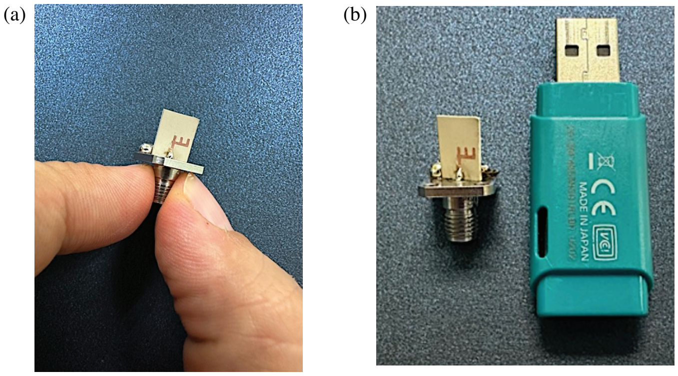

FIGURE 4. Fabricated prototype of the mmWave antenna. (a) The fabricated mmWave antenna with SMA connector, and (b) actual antenna size compared to a pen drive.

(300 kHz–44 GHz). Fig. 5 juxtaposes the simulated response (magenta dashed line) with the measured data (black solid line). The two traces follow the same trend, confirming the accuracy of the electromagnetic model. Deep nulls appear near 28 GHz and 38 GHz, corresponding to the 5G NR n257/n258 and n260 bands, respectively. At these resonances, the measured $|S_{11}|$ drops below -30 dB, indicating excellent impedance matching. The -10 dB bandwidth spans roughly 27.7–28.5 GHz ($\approx 2.8\%$ fractional bandwidth) and 36.2–42.1 GHz ($\approx 15.4\%$ fractional bandwidth), validating the antenna's dual-band, wideband capability. Minor frequency shifts of < 0.3 GHz between simulation and measurement are attributed to fabrication tolerances and coax-launch parasitics, yet the antenna comfortably meets the targeted 5G millimetre-wave spectrum.

Across the entire 24–46 GHz sweep the simulated curves (black) and measured curves (red/magenta) track one another closely, confirming that the fabricated prototype behaves as designed. In Fig. 6(a), the antenna delivers a peak simulated gain of ∼6.7 dBi at 26 GHz and maintains 4.5–5.8 dBi throughout most of the passband, while the measured gain follows the same trend with only a 0.4–0.8 dB penalty — an excellent agreement for millimetre-wave hardware. The two pink highlight bars mark the intended 5G n257/n258 (around 28 GHz) and n260 (around 38 GHz) channels; within these windows the realised gain remains above 4.3 dBi, comfortably meeting typical handset front-end requirements. Fig. 6(b) shows that radiation efficiency likewise stays high: simulations predict 95–99%, and measurements confirm $\geq 92\%$ except for a narrow dip to $\sim 86\%$ near 38 GHz, which still exceeds the 80% benchmark often cited for practical mm-wave antennas. Collectively, the plots verify that the proposed structure offers stable, high-efficiency radiation with only minor fabrication-induced degradation, validating the design methodology.

The proposed antenna demonstrates stable radiation characteristics at both 28 GHz and 38 GHz, as shown in Fig. 7. In the E-plane ($\theta = 0°$), the patterns at 28 GHz exhibit a broadside radiation profile with good consistency between the simulated and measured results, while at 38 GHz, slight variations and additional lobes appear due to higher-frequency effects and measurement sensitivities. Similarly, in the H-plane ($\theta = 90°$), the antenna maintains a relatively directional pattern with close agreement between simulation and measurement, although minor discrepancies arise from fabrication tolerances and connector losses. These results in Fig. 7 confirm that the antenna maintains reliable radiation performance across both frequencies, validating the robustness of the design.

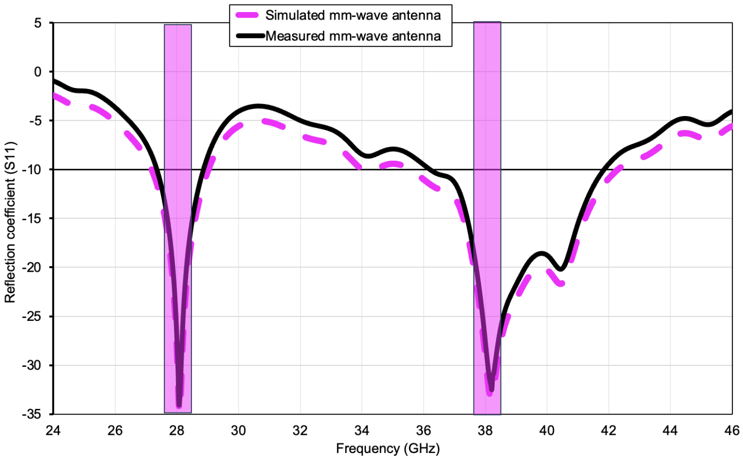

FIGURE 5. Predicted and experimented reflection coefficient ($|S_{11}|$) of the suggested millimeter-wave antenna highlighting good impedance matching across the 28 GHz (n257/n258) and 38 GHz (n260) 5G NR bands.

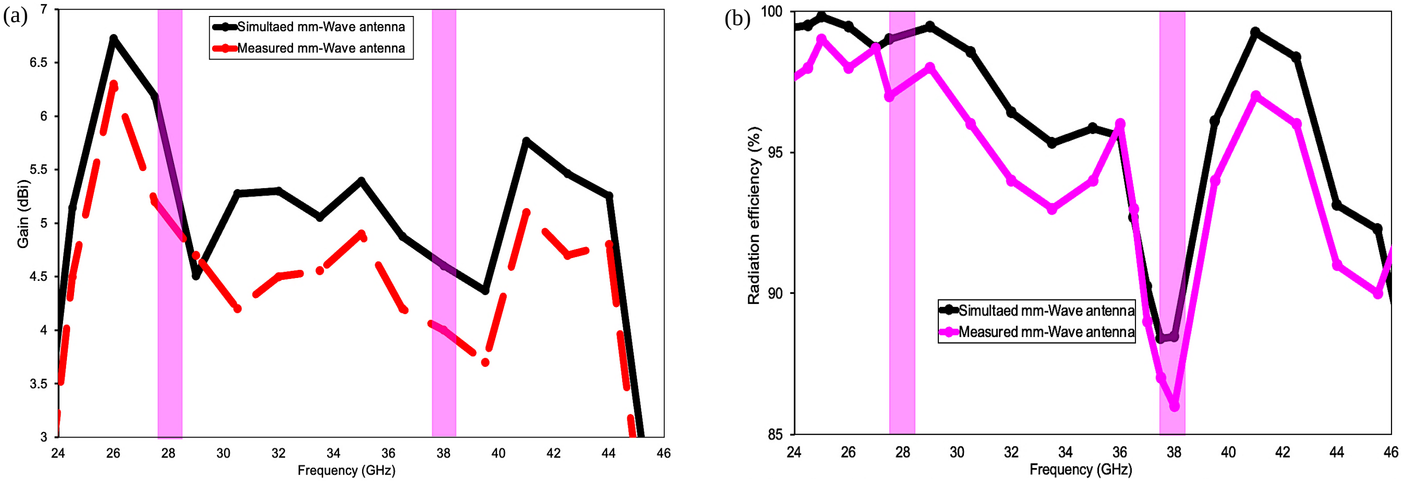

FIGURE 6. Predicted and exterminated outcomes of the fabricated mmWave antenna: (a) gain (dBi) and (b) radiation efficiency (%).

4. DATASET PREPARATION AND MACHINE-LEARNING MODELING FOR REFLECTION-COEFFICIENT PREDICTION OF A DUAL-BAND ANTENNA

Over the past decade, machine learning (ML) techniques have gained significant traction in the field of antenna design due to their ability to learn patterns from either observed measurements or simulated datasets. These techniques leverage a training process to model and predict antenna behavior effectively. In Machine Learning-Assisted model a computationally efficient surrogate model is developed using ML algorithms to estimate desired antenna characteristics throughout the design parameters. This model is trained on a dataset generated from strategically sampled evaluations of a computationally intensive simulation.

In general, machine learning is the process of deriving meaningful patterns from data through the construction of accurate predictive models. These models show strong potential in optimization applications; however, their performance is highly contingent on the quality and representativeness of the training data. This interdependence aligns ML closely with statistical analysis, as both disciplines focus on data-driven insights. Among various ML techniques, regression-based models are especially useful in accelerating optimization, as they offer rapid evaluations compared to traditional numerical solvers. Additionally, regression methods provide interpretability by identifying the influence of individual design parameters on the system's performance.

To enable the reliable machine-learning prediction of impedance and $|S_{11}|$, a substantial training dataset was required. Accordingly, a parametric sweep of the slot dimensions was carried out in CST, generating the necessary $|S_{11}|$ responses for the slotted patch antenna. The sweep produced 330 distinct samples spanning 26–30 GHz and 35–40 GHz. As antenna is operating at dual frequency bands of 28 GHz and 38 GHz. The wide range of frequencies for both the bands is considered to collect the variation in operating frequencies with the change in antenna dimensions. Every record comprises 1,000 discrete frequency points across the selected spectrum. Of the 300 total records, 264 (about 88%) were allocated

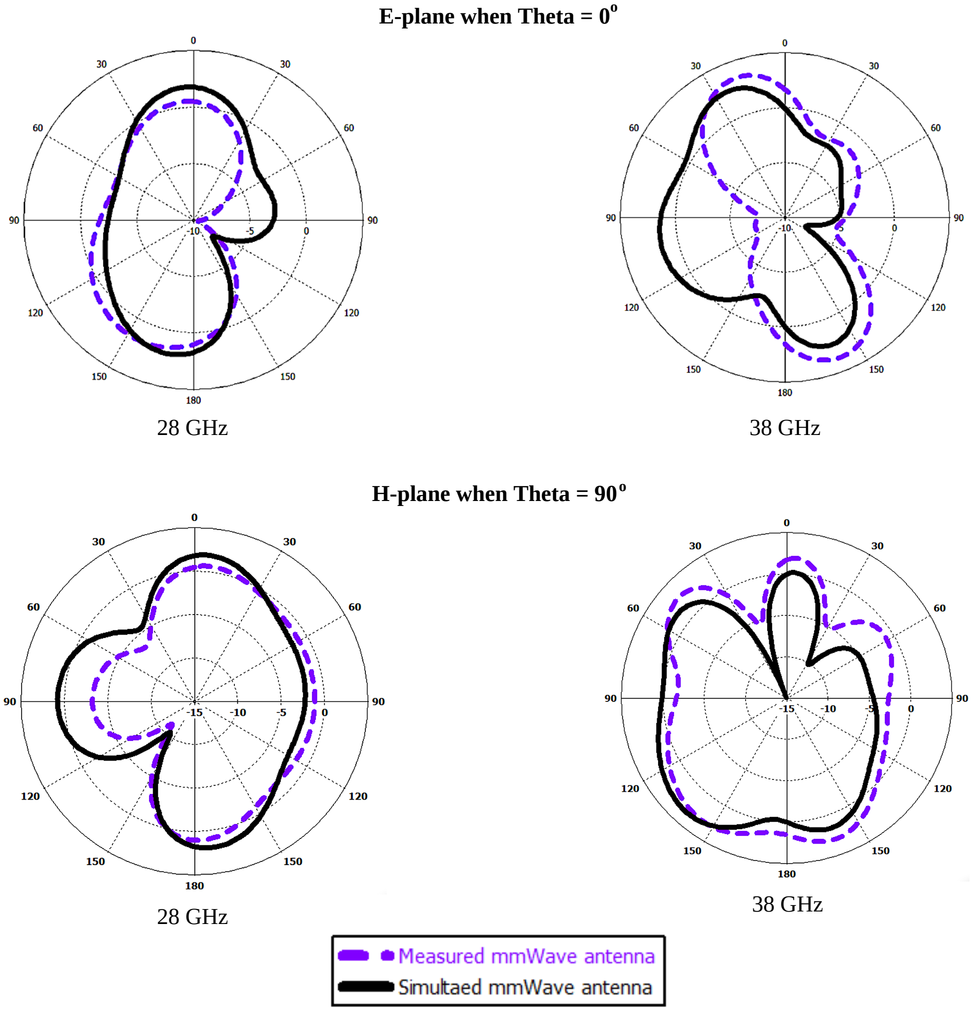
E-plane when Theta = 0°

28 GHz

38 GHz

H-plane when Theta = 90°

28 GHz

38 GHz

FIGURE 7. Simulated and measured radiation patterns of the proposed mmWave antenna at 28 GHz and 38 GHz in the E-plane ($\theta = 0^\circ$) and H-plane ($\theta = 90^\circ$).

for model training, while the remaining 66 were held out for validation.

The simulated dataset was first inspected for multicollinearity between frequency points and the corresponding $|S_{11}|$ values, since highly correlated inputs can degrade the performance of a machine-learning regressor. The resulting correlation matrix — visualised as a heat-map in Fig. 8 — reveals that $|S_{11}|$ exhibits strong correlation with its immediately neighbouring frequency samples, a consequence of the antenna's broadband and dual-band behaviour. To minimise redundant information and improve predictive accuracy, the dataset was pruned to the two most informative windows: 27–29 GHz and 37–39 GHz, yielding 500 evenly spaced frequency points. All other highly correlated frequencies were discarded before training.

In this study, a Random Forest (RF) regression algorithm is employed to fit the learning model and forecast key antenna performance metrics. Regression techniques are known for their computational efficiency and ability to identify the contribution of individual design variables to the predicted outcomes. Specifically, Random Forest operates as an ensemble technique: it constructs many decision trees and combines their individual outputs, which boosts both predictive accuracy and model generalisation.

The RF regression model operates through the following steps:

1. Bootstrapped Sampling: Generate multiple bootstrapped subsets from the original dataset, each serving as the training input for an individual decision tree.

2. Tree Construction: Build each decision tree by randomly selecting a subset of features at each node for splitting, promoting diversity among the trees.

3. Prediction Aggregation: Calculate the final predicted value by taking the mean of the outputs from all individual decision trees in the forest.

This ensemble learning approach enhances robustness and reduces the risk of overfitting, making it well-suited for modeling complex relationships in antenna design.

To implement the machine-learning workflow, the CST-generated dataset was split 80% for training and 20% for validation. The antenna optimisation problem involves N perfor-

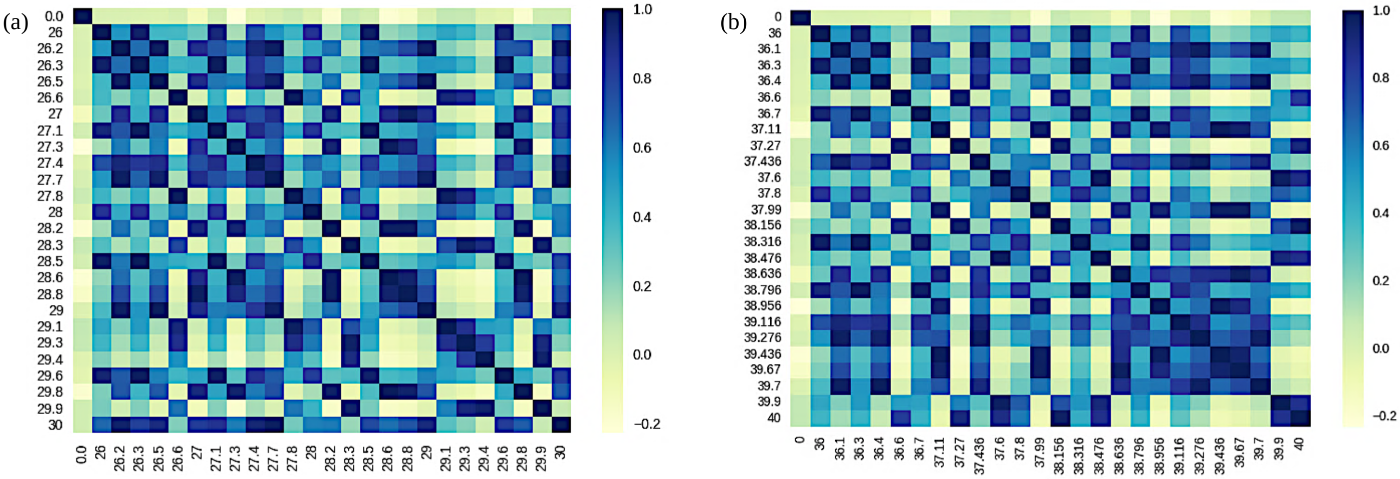

FIGURE 8. Heatmsap of the S_{11} correlation matrix (a) at 28 GHz, (b) at 38 GHz.

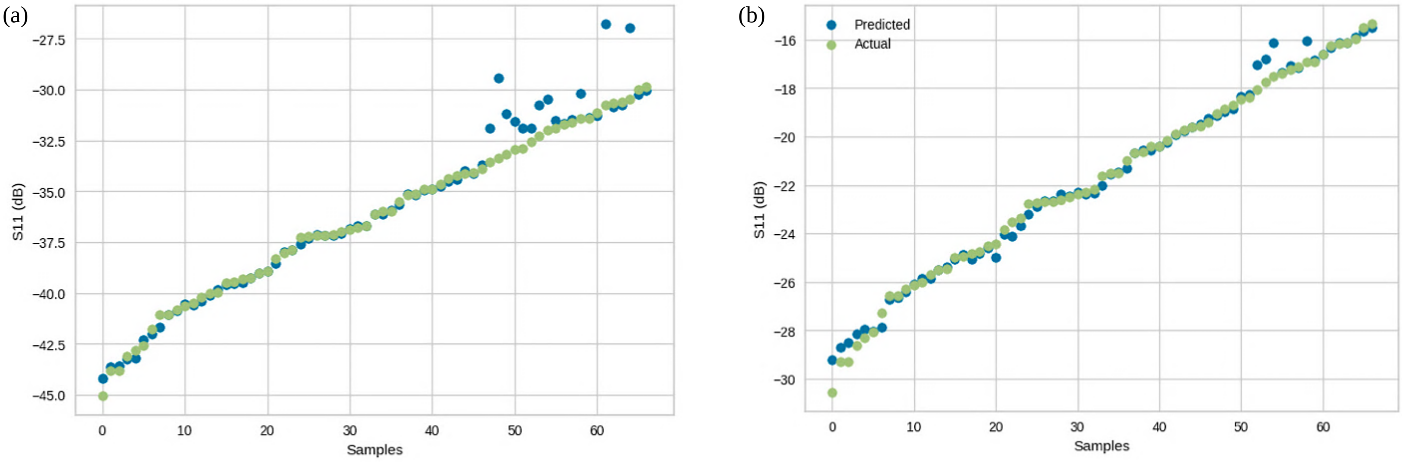

FIGURE 9. Actual and predicted values (a) at 28 GHz, (b) at 38 GHz.

mance objectives, so each sample can be expressed as $x_i \to y_{ij}$ $(j = 1, 2, ..., N)$. A statistical weighting scheme converts this multi-objective formulation into a single scalar target by assigning a weight to each objective and combining them into a composite score SSS. This weighted metric serves as the objective function for subsequent optimisation and is defined as follows:

$$S = \sum_{J=1}^{N} w_j y_j \tag{1}$$

Here, w_j represents the weight assigned to the jth objective y_j. To balance the influence of each objective, this weight is normalised by the mean value of y_j, as detailed in Equation (2).

$$w_j = \frac{\prod_{j=1}^{N} \sum_{1}^{n} \frac{y_{ij}}{N}}{\sum_{1}^{n} \frac{y_{ij}}{N}} \tag{2}$$

The learning phase derives a functional mapping $x_i \to S(w_j, y_j)$, where the composite score S is weighted by w_j so that it closely reflects the dominant objective y_j. Model fidelity is assessed with the coefficient of determination R^2; values approaching 1 signify an excellent fit, whereas values near 0 indicate a poor one. R^2 is calculated as follows:

$$\mathrm{R}^2 = 1 - \frac{\sum_{1}^{N} \left(y_i - y_i^{'}\right)^2}{\sum_{1}^{N} \left(y_i - y_i^{\wedge}\right)^2} \tag{3}$$

where y_i represents the observed value, $y_i^{'}$ the corresponding model prediction, and $y_i^{\wedge}$ the average of all observed values.

4.1. Prediction of Reflection Coefficient and Result Analysis

In this stage, the simulated $|S_{11}|$ magnitudes and corresponding geometric variables are fed into the machine-learning framework developed for the slotted microstrip patch. By sweeping the six key design dimensions S_1, S_2, S_3, K_1, K_2, and K_3, a comprehensive dataset is generated. Once the Random-Forest regressor is trained, it is used to predict $|S_{11}|$ for 67 unseen samples. Figs. 9(a)–(b) compare the predicted values with the simulated references at 28 GHz and 38 GHz, showing excellent agreement.

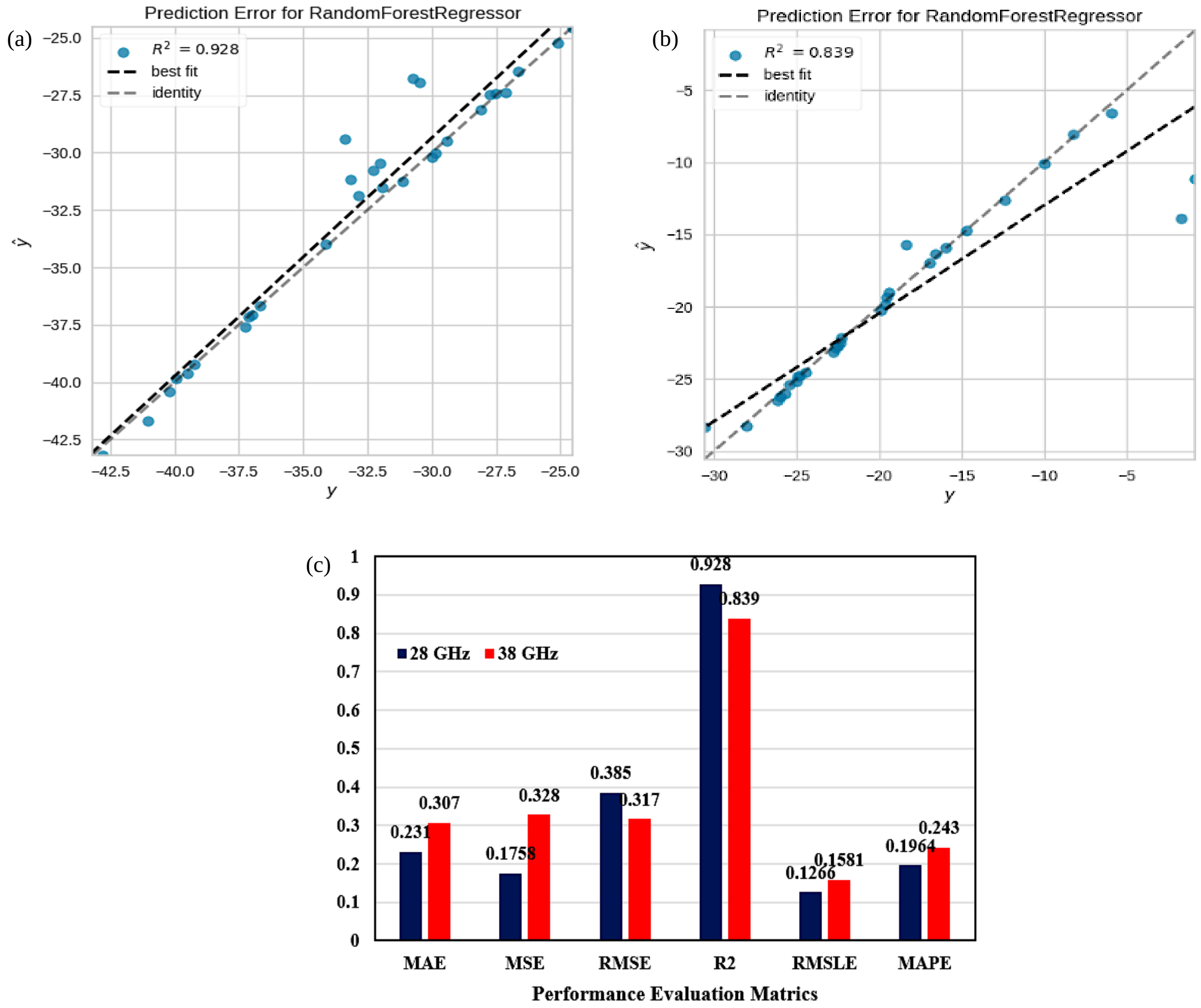

FIGURE 10. Model-fit plots and corresponding R^2 values: (a) 28 GHz, (b) 38 GHz, and (c) summary of performance metrics.

Model fidelity is quantified in Figs. 10(a)–(c) via best-fit trends, R^2 statistics, and error metrics. The bold dotted line denotes the regression fit, while the lighter band illustrates its confidence interval; a narrower spread between residuals and this line signals higher predictive accuracy. The model attains $R^2 \approx 0.928$ at 28 GHz and 0.839 at 38 GHz — values near or above 0.9 indicate an excellent match for reflection-coefficient estimation. The slightly lower R^2 at 38 GHz likely stems from greater variability in certain input features, which amplifies scatter in the target response. Even so, all error measures (MSE, MAE, RMSE, RMSLE, and MAPE) remain below 4%, confirming the model's strong predictive efficiency for the antenna under study.

To gauge the model's robustness in predicting $|S_{11}|$, a repeated n-fold cross-validation was carried out. Specifically, an eight-fold split was executed 15 times, and the average performance for each run was recorded. The resulting error trends for all repetitions are plotted in Fig. 11. During all the repeats error is varying below 0.5 for both the bands. An accuracy plot for n-fold performance is shown in Fig. 12. At 28 GHz, maximum accuracy is 0.98 for fold-3, and minimum accuracy is 0.86 for fold-2. At 38 GHz, maximum accuracy is 0.98 for fold-5, and minimum accuracy is 0.83 for fold-4. The results demonstrate that the model remains consistently stable across all cross-validation folds. Such accuracy is crucial for confidently adjusting design variables and precisely forecasting the antenna's reflection coefficient.

Table 2 summarises the model's $|S_{11}|$ forecasts alongside the corresponding prediction errors. By sweeping the antenna's geometric dimensions, different resonant conditions were generated, and $|S_{11}|$ was taken as the response variable for both target bands. The table reports 66 paired entries — simulated versus predicted — at 28 GHz and 38 GHz. In this set, the largest deviation occurs at 28 GHz, where the error reaches 14.45% for sample 254; the same sample shows a much smaller error of 2.74% at 38 GHz. Similarly, maximum prediction error at 38 GHz for the $|S_{11}|$ parameter is 12.84% (sample number 279) corresponding to prediction error of 2.04% for 28 GHz band.

The machine-learning model yields a peak $|S_{11}|$ prediction of -44.196 dB at 28 GHz (sample 234) and -29.064 dB at 38 GHz (sample 96). The simulated and predicted $|S_{11}|$ values along with their respective errors at 28 GHz and 38 GHz are shown in Fig. 13. The prediction error remains below 14% across all samples, and the predicted curves closely overlap

TABLE 2. Model forecasts and associated errors for return-loss and impedance metrics.

S. No.	Design parameters						38 GHz		28 GHz		Error (%)	Error (%)
	S_3	K_2	K_1	S_2	S_1	K_3	Simulated S11	Predicted S11	Simulated S11	Predicted S11	28 GHz	38 GHz
151	0.554	1.894	0.516	1.074	0.518	1.726	-30.57	-28.363	-45.07	-44.196	7.219%	1.940%
138	0.658	1.458	0.712	1.015	0.633	2.32889	-29.3	-29.033	-43.8	-43.635	0.912%	0.377%
22	0.704	1.907	0.572	1.01	0.489	1.664	-29.3	-29.064	-43.8	-43.563	0.806%	0.541%
0	0.686	1.8	0.632	1.001	0.483	1.933	-28.6	-28.603	-43.1	-43.234	0.010%	0.311%
134	0.558	1.88	0.617	1.012	0.531	1.808	-28.3	-28.224	-42.8	-43.172	0.267%	0.870%
4	0.686	1.778	0.573	0.992	0.49	1.86	-28.06	-28.302	-42.56	-42.292	0.861%	0.630%
9	0.67	1.5319	0.643	0.976	0.567	2.219	-27.29	-27.105	-41.79	-41.999	0.680%	0.501%
139	0.577	1.36173	0.558	0.987	0.559	1.863	-26.55	-26.833	-41.05	-41.672	1.066%	1.515%
147	0.652	1.366	0.586	0.9553	0.544	1.832	-26.55	-26.564	-41.05	-41.070	0.054%	0.049%
132	0.629	1.195	0.656	0.957	0.616	2.195	-26.3	-26.469	-40.8	-40.849	0.644%	0.121%
140	0.573	1.7	0.645	0.951	0.715	2.207	-26.13	-26.492	-40.63	-40.542	1.385%	0.216%
141	0.511	1.702	0.645	0.951	0.715	2.207	-25.99	-26.215	-40.49	-40.577	0.867%	0.215%
130	0.493	1.533	0.596	0.938	0.597	2.25	-25.69	-26.026	-40.19	-40.393	1.309%	0.505%
146	0.573	1.62	0.608	0.938	0.612	2.204	-25.5	-25.815	-40	-40.098	1.234%	0.245%
127	0.618	1.465	0.666	0.954	0.603	2.375	-25.45	-25.422	-39.95	-39.835	0.108%	0.287%
13	0.652	1.366	0.586	0.955	0.544	1.832	-24.99	-25.165	-39.49	-39.604	0.701%	0.289%
323	0.643	1.325	0.616	0.95	0.541	1.966	-24.93	-24.852	-39.43	-39.528	0.313%	0.250%
6	0.583	1.361	0.601	0.954	0.5789	1.895	-24.82	-24.762	-39.32	-39.499	0.234%	0.456%
145	0.647	1.362	0.586	0.94	0.556	1.942	-24.75	-24.549	-39.25	-39.241	0.811%	0.024%
12	0.653	1.24	0.622	0.938	0.5918	2.081	-24.5	-24.551	-39	-39.013	0.207%	0.034%
17	0.584	1.721	0.674	0.933	0.485	1.64	-24.43	-24.556	-38.93	-38.926	0.516%	0.009%
128	0.714	1.436	0.645	0.935	0.532	2.098	-23.821	-23.811	-38.321	-38.542	0.041%	0.576%
142	0.57	1.69	0.656	0.934	0.5011	1.835	-23.5	-23.516	-38	-37.953	0.066%	0.123%
18	0.524	1.672	0.635	0.927	0.64	2.228	-23.36	-23.401	-37.86	-37.867	0.176%	0.018%
135	0.586	1.184	0.616	0.921	0.609	2.03	-22.77	-23.131	-37.27	-37.590	1.583%	0.859%
258	0.555	1.288	0.622	0.925	0.657	2.103	-22.71	-22.753	-37.21	-37.302	0.191%	0.248%
143	0.592	1.29559	0.64	0.9169	0.542	1.8203	-22.69	-22.746	-37.19	-37.097	0.247%	0.251%
150	0.657	1.187	0.622	0.917	0.566	2.049	-22.67	-22.873	-37.17	-37.147	0.896%	0.063%
131	0.546	1.224	0.598	0.919	0.598	2.125	-22.62	-22.592	-37.12	-37.145	0.122%	0.067%
19	0.592	1.26	0.612	0.921	0.609	2.092	-22.5	-22.754	-37	-37.066	1.130%	0.177%
129	0.599	1.359	0.606	0.916	0.592	1.959	-22.37	-22.545	-36.87	-36.849	0.782%	0.057%
2	0.636	1.36	0.589	0.92	0.591	1.977	-22.3	-22.198	-36.8	-36.693	0.458%	0.291%
25	0.633	1.287	0.619	0.926	0.621	2.101	-22.17	-21.945	-36.67	-36.669	1.015%	0.003%
137	0.6	1.68	0.6	0.9	0.6	2	-21.63	-21.724	-36.13	-36.142	0.434%	0.033%
245	0.573	1.544	0.612	0.9012	0.568	2.26	-21.5	-21.666	-36	-36.118	0.773%	0.329%
10	0.586	1.228	0.606	0.9	0.584	2.103	-21.5	-21.457	-36	-35.936	0.202%	0.177%
148	0.594	1.284	0.629	0.915	0.554	1.923	-20.99	-21.104	-35.49	-35.638	0.545%	0.417%
243	0.624	1.206	0.636	0.914	0.633	2.193	-20.69	-20.760	-35.19	-35.142	0.338%	0.136%

16	0.565	1.279	0.599	0.903	0.619	2.14	-20.62	-20.651	-35.12	-35.169	0.151%	0.141%
23	0.639	1.334	0.614	0.907	0.564	2.015	-20.39	-20.470	-34.89	-34.913	0.393%	0.067%
8	0.603	1.319	0.631	0.91	0.588	2	-20.38	-20.426	-34.88	-34.884	0.224%	0.012%
136	0.613	1.256	0.621	0.902	0.651	2.19	-20.17	-20.301	-34.67	-34.730	0.651%	0.174%
300	0.622	1.311	0.613	0.914	0.651	2.13	-19.87	-20.254	-34.37	-34.494	1.931%	0.361%
133	0.583	1.894	0.617	1.074	0.715	2.207	-19.71	-19.995	-34.21	-34.421	1.446%	0.616%
284	0.647	1.458	0.573	1.015	0.597	2.207	-19.61	-19.835	-34.11	-33.971	1.150%	0.408%
144	0.653	1.907	0.643	1.01	0.612	2.25	-19.56	-19.353	-34.06	-34.137	1.057%	0.227%
11	0.584	1.8	0.558	1.001	0.603	2.204	-19.4	-19.037	-33.9	-33.691	1.870%	0.616%
7	0.714	1.88	0.586	1.012	0.544	2.375	-19.04	-18.906	-33.54	-31.896	0.703%	4.900%
15	0.57	1.778	0.656	0.992	0.541	1.832	-18.86	-18.828	-33.36	-29.417	0.171%	11.819%
149	0.524	1.5319	0.645	0.976	0.5789	1.966	-18.68	-18.746	-33.18	-31.190	0.352%	5.998%
304	0.586	1.36173	0.645	0.987	0.556	1.895	-18.46	-18.260	-32.96	-31.549	1.082%	4.280%
254	0.555	1.366	0.596	0.9553	0.5918	1.942	-18.37	-15.715	-32.87	-31.893	14.451%	2.971%
5	0.592	1.195	0.608	0.957	0.485	2.081	-18.06	-16.094	-32.56	-31.896	10.888%	2.041%
24	0.657	1.7	0.666	0.951	0.532	1.64	-17.76	-17.528	-32.26	-30.763	1.306%	4.639%
244	0.546	1.702	0.586	0.951	0.5011	2.098	-17.5	-17.239	-32	-30.479	1.491%	4.753%
250	0.592	1.533	0.616	0.938	0.64	1.835	-17.41	-17.396	-31.91	-31.536	0.082%	1.173%
256	0.599	1.62	0.601	0.938	0.609	2.228	-17.22	-17.260	-31.72	-31.677	0.233%	0.136%
20	0.636	1.465	0.586	0.954	0.657	2.03	-17.13	-17.142	-31.63	-31.479	0.073%	0.478%
305	0.586	1.366	0.622	0.955	0.542	2.101	-16.94	-17.011	-31.44	-30.196	0.416%	3.958%
337	0.594	1.325	0.674	0.95	0.566	2	-16.94	-17.010	-31.44	-31.396	0.413%	0.139%
247	0.624	1.361	0.645	0.954	0.598	2.26	-16.62	-16.376	-31.12	-31.277	1.468%	0.504%
279	0.565	1.362	0.656	0.94	0.609	2.103	-16.24	-16.207	-30.74	-26.791	0.204%	12.845%
302	0.639	1.24	0.635	0.938	0.592	1.923	-16.18	-15.949	-30.68	-30.830	1.430%	0.487%
253	0.603	1.721	0.616	0.933	0.591	2.193	-16.13	-16.101	-30.63	-30.736	0.178%	0.345%
238	0.613	1.36	0.622	0.92	0.621	2.14	-15.97	-15.904	-30.47	-26.960	0.414%	11.518%
248	0.622	1.287	0.64	0.926	0.6	1.86	-15.5	-15.475	-30	-30.220	0.164%	0.733%
317	0.592	1.68	0.622	0.9	0.568	2.219	-15.36	-15.430	-29.86	-30.028	0.453%	0.562%

TABLE 3. Runtime and resource requirements of the proposed approach.

Model	Model Configurations	Time
Single CST EM Simulation With A Low-Resolution Mesh	• 15 cells per wavelength • 20 cells along the longest box edges • Local refinement: 20% of maximum cell size near the structure • Total mesh cells: 146 832	160 s
Single Execution of A Random-Forest Regressor On Google Colab	Python model trained on 330 CST-generated samples	0.2–0.4 s

with the simulated ones. This strong agreement demonstrates the effectiveness of the machine learning algorithm in capturing the antenna design behavior. The Random Forest approach, in particular, proves to be an accurate and efficient tool for analyzing $|S_{11}|$ and guiding antenna design.

Table 3 presents the runtime profile of the entire workflow. Full-wave reference data were produced in CST following the cost metrics reported in [17–19]. Simulations were run on a workstation with 16 GB RAM and an Intel® Core™ i5-8365U (1.60 GHz), where 330 low-mesh solutions each required about

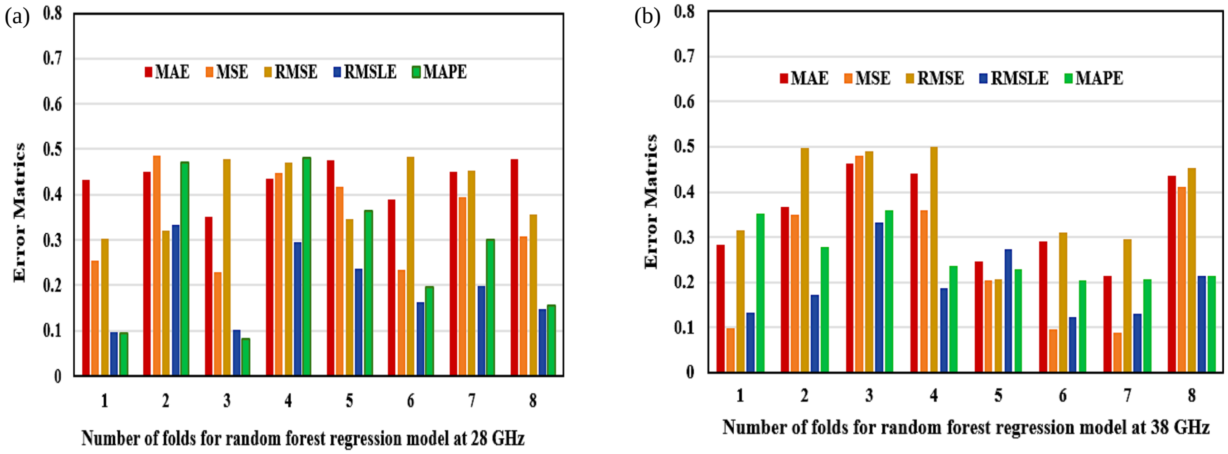

FIGURE 11. Consolidated error profiles — MAE, RMSE, MAPE, and R^2 — averaged over 15 independent runs of eight-fold cross-validation for the predicted $|S_{11}|$ responses at 28 GHz and 38 GHz.

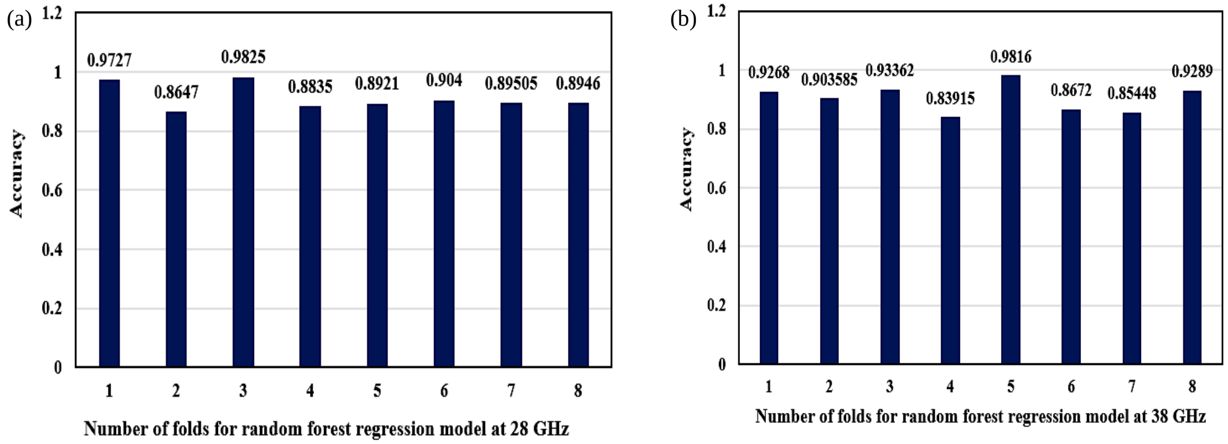

FIGURE 12. Summary of a repeated 8-fold cross validation accuracy.

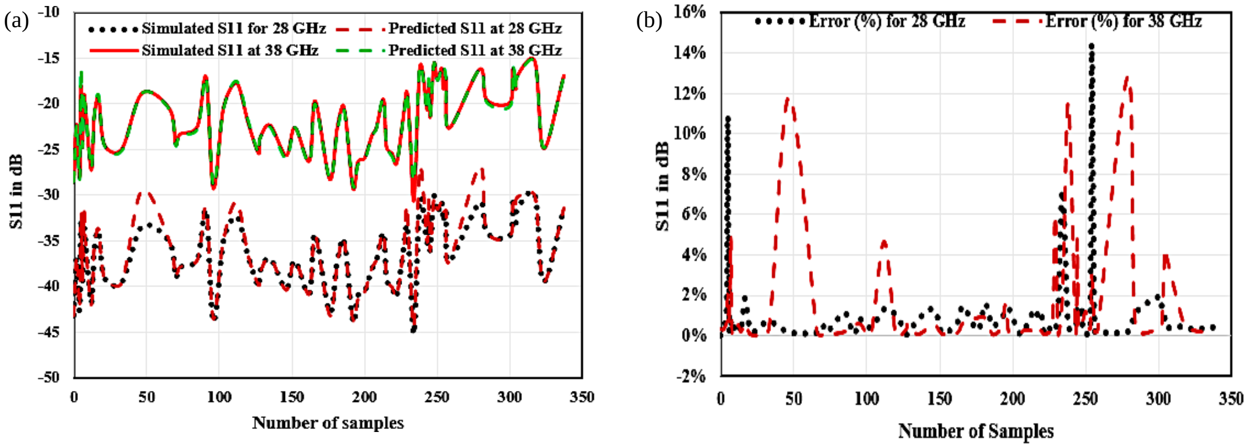

FIGURE 13. (a) Curves for simulated and predicted S_{11} parameters for different dimension of antenna as number of samples, (b) error in computed and predicted parameters.

155 s. By comparison, the Random-Forest surrogate was executed on Google Colab and occupied only $\sim$ 200 MB of memory. End-to-end processing — 0.3 s to train on 264 samples and 0.1 s to predict the remaining 66 — finished in roughly 0.4 s. This three-orders-of-magnitude speed-up shows that the ML-based approach can deliver near-instantaneous antenna evaluations, whereas the computational load of conventional electromagnetic (EM) simulation precludes real-time deployment. This rapid response demonstrates the efficiency of machine learning for analytical computations in antenna systems. In

TABLE 4. Comparison with related work.

Ref.	Antenna Design	Bands (GHz)	ML Algorithm	Predicted/Measured Feature	Key Results
[20]	2-element microstrip patch with DGS (measured)	28/38	–	Measured $\lvert S_{11}\rvert$	$\lvert S_{11}\rvert < -10$ dB; Isolation > 27 dB; Gain 6.2 dBi (28 GHz), 7 dBi (38 GHz)
[21]	Meandered slot patch	2.0–3.0	RF, XGB	$\lvert S_{11}\rvert$, impedance	$R^2 \approx 0.98$; MAE < 0.5 dB; 10-fold CV validated
[22]	Microstrip line-fed DRA	3.3–3.65	RF, DT, XGB, KNN, ANN, KBNN	$\lvert S_{11}\rvert$	RF $\approx 91\%$, DT $\approx 97\%$; KBNN stabilizes ANN predictions
[23]	Dual-band microstrip patch	8.35–14.15	CNN, LR, RFR, DTR, XGB	Resonant frequency	DTR best: MSE $= 0.71\%$, MSE $= 5.63\%$, Var score $\approx 99.7\%$
[24]	Microstrip patch	2.4–5.0	RF, XGB Ensemble	$\lvert S_{11}\rvert$	RF: 79.9%, XGB: 83.9% accuracy
This work	Coin-sized dual-band microstrip (slotted)	**28/38**	Random Forest	$\lvert S_{11}\rvert$	**MAE ≤ 0.7 dB, $R^2 \approx 0.9$, $150\times$ faster than EM solver; Peak gain 3.8/4.1 dBi**

contrast, the high time complexity of EM-based simulations limits their applicability in real-time scenarios.

The comparison of existing literature on antenna parameter forecasting employing machine learning is explored and summarized in Table 4.

5. CONCLUSIONS

A $10 \times 8 \times 0.64\,\text{mm}^3$ antenna on Rogers 6010 LM delivers $\lvert S_{11}\rvert \leq -10$ dB over 26.5–29.9 GHz and 37.2–39.7 GHz, with peak gains of 3.8 dBi and 4.1 dBi. A random-forest surrogate, trained on 330 full-wave samples, predicts frequency-resolved $\lvert S_{11}\rvert$ with $<$ 0.7 dB MAE ($\text{R}^2 = 0.93$ at 28 GHz, 0.84 at 38 GHz) and cuts evaluation time from 155 s to 0.1 s — over $150\times$ faster than EM sweeps. Cross-validation confirms stability, and feature-importance ranking pinpoints the key geometry levers for dual-band matching. This hardware-and-ML pairing enables real-time impedance assessment and rapid optimisation of coin-sized mmWave antennas, offering a scalable route for future instrumentation, sensing, and coin-sized radio frequency front-end designs.

ACKNOWLEDGEMENT

The author gratefully acknowledges Universiti Teknikal Malaysia Melaka (UTeM) and the Ministry of Higher Education Malaysia (MOHE) for providing the essential fabrication materials, including the Rogers 6010LM substrate. Appreciation is also extended to Universiti Teknologi Malaysia (UTM) for granting access to its mm-wave measurement facilities.

REFERENCES

[1] Rappaport, T. S., S. Sun, R. Mayzus, H. Zhao, Y. Azar, K. Wang, G. N. Wong, J. K. Schulz, M. Samimi, and F. Gutierrez, "Millimeter wave mobile communications for 5G cellular: It will work!" *IEEE Access*, Vol. 1, 335–349, 2013.

[2] Abdullah Al-Gburi, A. J., "5G MIMO antenna: Compact design at 28/38 GHz with metamaterial and SAR analysis for mobile phones," *Przeglad Elektrotechniczny*, Vol. 2024, No. 4, 171–174, 2024.

[3] Jemaludin, N. H., A. J. A. Al-Gburi, R. H. Elabd, T. Saeidi, M. F. Akbar, I. M. Ibrahim, and Z. Zakaria, "A comprehensive review on MIMO antennas for 5G smartphones: Mutual coupling techniques, comparative studies, SAR analysis, and future directions," *Results in Engineering*, Vol. 23, 102712, Sep. 2024.

[4] Tiwari, R. N., O. S. Sai, D. Sharma, M. S. Kumar, P. Singh, P. Kumar, C. Sreemanya, and S. Rajasekaran, "A low-profile dual-band millimeter wave patch antenna for high-speed wearable and biomedical applications," *Results in Engineering*, Vol. 24, 103212, Dec. 2024.

[5] Ullah, H., H. F. Abutarboush, A. Rashid, and F. A. Tahir, "A compact low-profile antenna for millimeter-wave 5G mobile phones."

[6] Liang, Q., H. Aliakbari, and B. K. Lau, "Co-designed millimeter-wave and sub-6 GHz antenna for 5G smartphones," *IEEE Antennas and Wireless Propagation Letters*, Vol. 21, No. 10, 1995–1999, Oct. 2022.

[7] Oh, J., B. Kim, S. Yoon, K. Kim, E. J. Sung, and J. Oh, "High-gain millimeter-wave antenna-in-display using non-optical space for 5G smartphones," *IEEE Transactions on Antennas and Propagation*, Vol. 71, No. 2, 1458–1468, Feb. 2023.

[8] Khabba, A., S. Mohapatra, L. Wakrim, F. Ez-zaki, S. Ibnyaich, and A. Zeroual, "Multiband antenna design with high gain and robust spherical coverage using a new 3D phased array structure

for 5G mobile phone mm-Wave applications," *Analog Integrated Circuits and Signal Processing*, Vol. 110, No. 2, 331–348, 2022.

[9] Jain, P., P. K. Sahoo, A. D. Khaleel, and A. J. A. Al-Gburi, "Enhanced prediction of metamaterial antenna parameters using advanced machine learning regression models," *Progress In Electromagnetics Research C*, Vol. 146, 1–12, 2024.

[10] Rana, M. S., S. M. R. Islam, and S. Sarker, "Machine learning based on patch antenna design and optimization for 5G applications at 28 GHz," *Results in Engineering*, Vol. 24, 103366, 2024.

[11] Yadav, S. K., A. Gupta, V. Kumar, D. K. Garg, and A. J. A. Al-Gburi, "Prediction of axial ratio using machine learning (ML) for a dual-band circularly polarized dielectric resonator antenna (DRA)," *Chinese Journal of Physics*, Vol. 96, 1364–1384, 2025.

[12] Ramasamy, R. and M. A. Bennet, "An efficient antenna parameters estimation using machine learning algorithms," *Progress In Electromagnetics Research C*, Vol. 130, 169–181, 2023.

[13] Huang, C.-H., H.-H. Tsao, C.-C. Hsu, A. Ali, and S.-Y. Liao, "Antenna structure prediction and optimization based on machine learning and grid search," in *2024 IEEE International Workshop on Electromagnetics: Applications and Student Innovation Competition (iWEM)*, 1–3, Taoyuan County, Taiwan, 2024.

[14] Jain, R., R. Ramya, V. V. Thakare, and P. K. Singhal, "Design and analysis of antenna through machine learning for next-generation IoT system," *Discover Internet of Things*, Vol. 5, No. 1, 1–15, 2025.

[15] Abdelhamid, A. A. and S. R. Alotaibi, "Robust prediction of the bandwidth of metamaterial antenna using deep learning," *Computers, Materials & Continua*, Vol. 72, No. 2, 2305–2321, 2022.

[16] Gajbhiye, P. A., S. P. Singh, and M. K. Sharma, "A comprehensive review of AI and machine learning techniques in antenna design optimization and measurement," *Discover Electronics*, Vol. 2, No. 1, 46, 2025.

[17] Koziel, S., M. A. Belen, A. Çalişkan, and P. Mahouti, "Rapid design of 3D reflectarray antennas by inverse surrogate modeling and regularization," *IEEE Access*, Vol. 11, 24 175–24 184, 2023.

[18] Koziel, S. and A. Pietrenko-Dabrowska, "On nature-inspired design optimization of antenna structures using variable-resolution EM models," *Scientific Reports*, Vol. 13, No. 1, 8373, 2023.

[19] Koziel, S., A. Pietrenko-Dabrowska, and L. Golunski, "Globalized knowledge-based, simulation-driven antenna miniaturization using domain-confined surrogates and dimensionality reduction," *Applied Sciences*, Vol. 13, No. 14, 8144, 2023.

[20] Thakur, E., A. Gupta, M. K. Abdulhameed, A. D. Khaleel, and A. J. A. Al-Gburi, "Microstrip antenna with two elements and defected ground structure for 5G mobile applications at 28/38 GHz," *Progress In Electromagnetics Research C*, Vol. 146, 177–185, 2024.

[21] Gupta, A., V. Kumar, D. K. Garg, and A. J. A. Al-Gburi, "Machine learning-based reflection coefficient and impedance prediction for a meandered slot patch antenna," *Materials Science in Semiconductor Processing*, Vol. 188, 109245, 2025.

[22] Singh, O., M. R. Bharamagoudra, H. Gupta, A. K. Dwivedi, P. Ranjan, and A. Sharma, "Microstrip line fed dielectric resonator antenna optimization using machine learning algorithms," *Sādhanā*, Vol. 47, No. 4, 226, 2022.

[23] Haque, M. A., N. Sarker, N. S. S. Singh, M. A. Rahman, M. N. Hasan, M. Islam, M. A. Zakariya, L. C. Paul, A. H. Sharker, G. E. M. Abro, *et al.*, "Dual band antenna design and prediction of resonance frequency using machine learning approaches," *Applied Sciences*, Vol. 12, No. 20, 10505, 2022.

[24] Jain, R., P. Ranjan, P. K. Singhal, and V. V. Thakare, "Estimation of S_{11} values of patch antenna using various machine learning models," in *2022 IEEE Conference on Interdisciplinary Approaches in Technology and Management for Social Innovation (IATMSI)*, 1–4, Gwalior, India, 2022.